Powder Technology 458 (2025) 120906

Contents lists available at ScienceDirect

Powder Technology

journal homepage: www.journals.elsevier.com/powder-technology

Novel nanoparticle mixing approach for the production of solid-state battery hetero-agglomerates in vibrated fluidized beds

Zhi Cheng Hua [a,*], Finn Frankenberg [b], Maximilian Kissel [c], Jürgen Janek [c], Arno Kwade [b], Stefan Heinrich [a]

[a] Institute of Solids Process Engineering and Particle Technology, Hamburg University of Technology, Germany
[b] Institute of Particle Technology, Technical University of Braunschweig, Germany
[c] Institute of Physical Chemistry & Centre for Material Research, Justus-Liebig-University Gießen, Germany

HIGHLIGHTS

- Microjet-assisted vibrated fluidized bed enhances nanoscale mixing in solid-state battery materials.
- Optimal mixing achieved by combining high-velocity microjets with vibrated fluidization.
- Significant improvement in homogeneity and electrochemical performance of $LiFePO_4$-Li_3InCl_6-carbon black compo sites.
- SEM and FIB-SEM confirm improved agglomerate formation and particle exchange at the nanoscale.

GRAPHICAL ABSTRACT

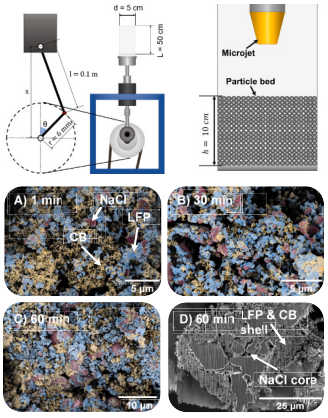

ARTICLE INFO

Keywords:
Heteroagglomerates
Nanoparticle Mixing
Vibrated Fluidized Bed
Microjet Assistance
Solid-state battery (ASSB)

ABSTRACT

A vibrated fluidized bed with microjet assistance is utilized to mix heterogeneous submicron-sized battery materials. This process aims to improve the homogeneity and electrochemical performance of a solid-state cathode composite consisting of $LiFePO_4$ (LFP), Li_3InCl_6 (LIC) and carbon black (CB). A downwards directed microjet was employed to enhance fluidization and mixing quality. The research involved a parametric study, examining various vibration intensities, microjet nozzle sizes, and fluidization times to determine the optimal conditions for achieving a homogeneous composite on the microscale. Scanning electron microscope (SEM) and focused ion beam SEM (FIB-SEM) imaging were used to assess the mixing quality and confirm the formation of hetero-agglomerates. Assisted fluidization alone produces composites with inferior mixing quality, whereas a microjet significantly improves mixing. Electrochemical testing reveals that a vibrated fluidized bed alone is inadequate for mixing submicron-sized particles for battery applications, whereas the microjet enables the mixing and ionically bound active material.

* Corresponding author.
E-mail address: zhi.cheng.hua@tuhh.de (Z.C. Hua).

https://doi.org/10.1016/j.powtec.2025.120906
Received 2 October 2024; Received in revised form 27 February 2025; Accepted 9 March 2025
Available online 14 March 2025

1. Introduction

The need for high performance batteries is steadily growing due to the increasing demand for electrochemically stored energy [1,2]. One possible solution to cover this demand, which gained a lot of attention due to its potential, are all-solid state-batteries (ASSBs) [3]. In contrast to conventional batteries such as lithium-ion batteries (LIBs), ASSBs do not contain a liquid electrolyte, but a solid electrolyte. It is inherently safer due to the lack of volatile organic compounds that are used as electrolytes, making them less prone for thermal runaway and flammability [4]. In addition, due to the use of a lithium metal anode, the energy density of an ASSB can be improved up to 70 % (volumetric) and 40 % (gravimetric) compared to LIBs, making the research on ASSBs worthwhile [4,5].

Conventional LIB cathodes consist of an active material (AM), binder and conductive additives like carbon black (CB) that increase the electronic conductivity. The liquid electrolyte, which dissolves a lithium salt like lithium hexafluorophosphate, ensures the ionic transport of lithium [6]. The fluid nature of the electrolyte in conventional LIB leads to a filling of the porous electrode structure, ensuring contact with the AM, and offering good ionic conductivity within the cathode [7,8]. In ASSBs the solid electrolyte has to provide the ionic conductivity and the connection within the ionically conducting network is achieved by interparticular heterocontacts, making the mechanical contact with the active material crucial [8].

One major challenge for ASSBs is to produce a cathode with low interfacial resistance, in which the active material is ionically connected with the solid electrolyte [9–11]. This challenge could be circumvented by functional mixing and high normal and shear forces, which lead to breakage of homoagglomerates or larger primary particles and thus result in contacts between different particle species (heterocontacts) of the ASSB cathode materials. The influence of normal and shear force acting in a high-intensity ring shear mixer on ASSB cathode composite consisting of submicron-sized AM $LiFePO_4$ (LFP), solid electrolyte Li_3InCl_6 (LIC), and carbon black (CB) as conductive additive was already investigated [12]. It was found that the electrochemical performance of the ASSB is significantly influenced by the normal and shear stress intensity. High stress-intensities lead to high degrees of solid electrolyte (SE) deagglomeration and small SE particles, resulting in a high number of heterocontacts and thus improved electrochemical performance. Previous research demonstrated that small SE particles ensure an improved connection of the AM to the ionic network [9,13]. Moreover, the addition and premixing of the solid electrolyte in the cathode composite can improve the electrochemical performance significantly, increasing the partial ionic conductivity within the cathode [14,15].

There have been many attempts to fabricate cathode composites for ASSBs on a lab scale, but still unsolved challenges remain for the large scale production [8,16,17]. The production processes must be scalable and the product quality must be robust. As the ASSB has to compete with conventional LIBs, the processes have to be automated and easy to implement, while ensuring the quality of the product [8]. For ASSBs as well as for LIBs, the focus has shifted from a wet, slurry-based production to a dry production chain, making the production safer due to the lack of volatile organic compounds and reducing the CO_2 footprint at the same time [8].

In the present work, the scalable and dry production of ASSB cathode composites in a vibrated fluidized bed consisting of LFP [18,19] as the AM, CB as conductive additive and sodium chloride (NaCl) as a substitute material for suitable SE is investigated. Besides using the substitute, mixing tests are carried out on the relatively moisture-tolerant and highly ion-conductive solid electrolyte LIC [20–22]. The dry mixing is realized in a self-built vibrated fluidized bed with jet assistance. Mixing parameters as well as process parameters like jet distance, nozzle diameter, vibration intensity and processing time are investigated.

Different strategies, including sieving and vibration, were employed to facilitate fluidization efficiency, which was evaluated based on the measurement of the weight normalized bed pressure drop. Moreover, the minimal fluidization velocity of LFP, LIC, NaCl, and CB in a dry environment across varying vibration velocities was investigated. Mixing experiments were conducted to generate composites, with subsequent assessments of particle morphology, mixing degree, and electronic powder conductivity. Furthermore, the impact of a downward-pointed high-velocity microjet was explored, focusing on understanding its mechanism and effect on solid electrolyte and CB deagglomeration as well as AM distribution. These aspects all influence the electrochemical performance of an ASSB, which was shown by electrochemical testing of full ASSB cells.

2. Scientific background

2.1. Fluidization of fine and ultrafine particles

Fluidized beds offer several advantages, including efficient heat transfer, uniform mixing, and accelerated reaction times. However, when dealing with small cohesive particles, known as Geldart C particles, the high ratio of interparticular forces (such as van der Waals, capillary, and electrostatic forces) to body forces (like gravitation) leads to cohesion and agglomeration, impeding proper fluidization [23]. Consequently, issues like segregation, plug flows, and particularly channelling, suspected to cause defluidization, have been frequently reported [23–27]. Studies by Kamphorst et al. identified channelling as the primary cause of poor fluidization [27]. As a result, external assistance is necessary to fluidize cohesive powders. Various methods, such as vibration, pulsated gas flows, sound-vibration, magnetic assistance, and microjet fluidization have been applied to counter defluidization. Notably, microjet fluidization has proven to significantly enhance the fluidization quality [25,28].

If fluidization was possible, Geldart C particles would fluidize as agglomerates instead of primary particles. Despite then typically falling under the Geldart A classification with diameters up to about 100 μm, agglomerates have a soft nature that complicates size measurements due to continuous de- and reagglomeration during fluidization [25,26,29]. Moreover, the elusive nature of size distribution endures, potentially differing from its fluidized state, and further varying within the bed height during fluidization. Agglomerates may break down or change their shape and size distribution, which makes the measurement of agglomerate size distributions difficult [30]. The fluidization quality of fine and ultra-fine particles can be monitored through the measurement of relative bed expansion, elutriation, minimal fluidization velocity, bubbling behavior and by analysing the pressure drop [29,31].

2.2. Mixing of fine and ultrafine particles

Fernandez-Diaz et al. provide a comprehensive examination of diverse mixing methodologies employed in the production of solid cathode composites, encompassing both dry and wet methods to process solid state composites [32]. However, the use of fluidized beds is not discussed. For a detailed exploration on nanofluidization and including their mixing efficiencies with different fluidization techniques, Van Ommen et al. offer an insightful review [25]. This study incorporates various techniques, including the use of tracers in conjunction with visual observation, as well as electron microscopic methods such as light microscopy, SEM-EDX, and TEM-EELS to evaluate the mixing quality.

In this contribution we differentiate between macromixing, i.e. the homogenization at the bulk level, and the micromixing. The micromixing involves changes in the morphology of agglomerates, aggregates and primary particles. The macromixing is often quantified through a mixing index or variance, indicating the homogeneity at the bulk level. The micromixing is often expressed in regards to a smaller scale than macromixing and is affected by the internal structure of individual primary particles or clusters. The assessment of the micromixing of different particulate materials is done through imaging techniques such

as SEM, AFM, TEM, FIB-SEM, and SEM-EDX, or by evaluating the end-use properties [33]. An updated review by Kamphorst et al. delivers a more recent and detailed classification of nanofluidization alongside an array of assisting methods [24]. Hakim et al. observed that vibro-fluidization of diverse nanoparticle-based agglomerates results in complex structured formations. Their findings indicate a continuous cycle of agglomerate breakage and reagglomeration during fluidization [34]. There have been various attempts to describe the mixing of nanoparticles in fluidized beds, including in vibrated fluidized beds, rotating fluidized beds, sound assisted fluidized beds and spouted beds [35]. Quevedo et al. qualitatively confirmed that particles only mixed on a microscale (presumably up to 1000 μm) [25,28]. Contrary, a secondary high velocity gas flow, a microjet, that is pointed downwards (see Fig. 2) was able to break down homoagglomerates, resulting in agglomerates that had exchanged nanoparticles, leading to a mixing on the nanoscale (presumably up to 1 μm), which was later confirmed via TEM EELS [28].

However, it is still unclear to which extent a vibrating fluidized bed or a nozzle-assisted fluidized bed is capable of producing well-mixed particle systems consisting of several types of particles in the submicron or nanoscale. Within the scope of this work it will be investigated if the used battery materials can be fluidized and mixed. Further, this study focuses on mixing in a laboratory-scale vibrating and nozzle-assisted fluidized bed to investigate the fluidization of the mixing behavior. It is investigated whether and to what extent agglomerates deagglomerate and subsequently reagglomerate, how the jet influences this or enhances the deagglomeration and whether the process is suitable for the production of cathode composites in ASSBs.

3. Materials and methods

3.1. Construction of the vibrated fluidized bed

A vibrated fluidized bed plant was constructed to investigate the fluidization behavior. Differential pressure signals were measured between the distributor plate and the bed using low pressure transducers (PX165 pressure transducers, Omega Engineering GmbH, Germany) in conjunction with a data acquisition system (USB-DAQ 6001, National Instruments, USA), that records the pressure signal with a frequency of either 1 Hz or 2500 Hz. This enables the capture and denoising of vibration induced signals. Nitrogen 5.0 was used as a fluidization gas. Two mass flow controllers (MFC) that supply 0 L/min–0.5 L/min and 0.5 L/min–25 L/min (El-Flow Select, Bronkhorst GmbH, Germany) were used to control the superficial gas velocity. The fluidized bed chamber is a polycarbonate tube with a diameter of 5 cm and a length of 50 cm. For the distributor plate, a sintered steel plate (SIKA-R with 5 mm thickness and 10 μm pore size, GKN Sinter Metals GmbH, Germany) was used to disperse the fluidization gas and to prevent the fine particles of falling into the windbox.

The vibration was realized through the actuation of a plate with a rod, connected to the fluidized bed, attached eccentrically to the plate, determining the amplitude of the vibration (see Fig. 1). A linear shaft was used to ensure strictly vertical vibration. A frequency variator controls the vibration frequency, and an additional toothed belt system provides further control of the frequency.

In this experimental setup, a key component is the piston-crank mechanism, which facilitates the conversion of rotational motion into translational motion, inducing vibrations into the fluidized bed. The mechanism consists of a rod of length l, which is positioned eccentrically on the plate with a distance r that determines the amplitude of the vibration. The rod rotates about a fixed pivot, driving the connecting rod and the piston in a reciprocating linear motion. The angle made by the rod with its initial position is represented as $\theta = \omega \bullet t$. The amplitude of the vibration r was set constant to be $r = 6 \bullet 10^{-3}$ m and the length of the rod was $= 0.1$ m. Using the law of cosines, the current position x of the piston from its mean position can be expressed through Eq. (1).

$$l^2 = r^2 + x^2 - 2rxcos(\theta) \tag{1}$$

By differentiating x with respect to the time get an expression for the velocity v:

$$v = \frac{dx}{dt} = -\frac{r\omega sin(\theta)}{1 + cos(\theta)}x \tag{2}$$

To calculate the acceleration a, v is differentiated with respect to t.

$$a = \frac{dv}{dt} = -\frac{-r\omega xcos(\theta)(1 + cos(\theta)) + r\omega sin(\theta)x\omega sin(\theta) + r\omega sin(\theta)(v)}{(1 + cos(\theta))^2} \tag{3}$$

The acceleration profile is periodic due to the cyclic nature of the crank's rotation, producing an approximately sinusoidal displacement of the piston. The acceleration can be plotted based on Eq. (3).

As shown in Fig. 1, the acceleration profile of the used setup is approximately equal to a sinusoidal function with the same amplitude. Despite there being a slight difference in the acceleration, especially at the lower peaks, the motion shall be assumed to be sinusoidal in this contribution. Although it might seem trivial, having a sinusoidal acceleration may not necessarily be the case for any piston crank machine of this kind, especially if the crank length is of similar size as the chosen length of the eccentricity (see Fig. 1 example setup acceleration).

The jet assistance was realized by pointing a metal pipe into the

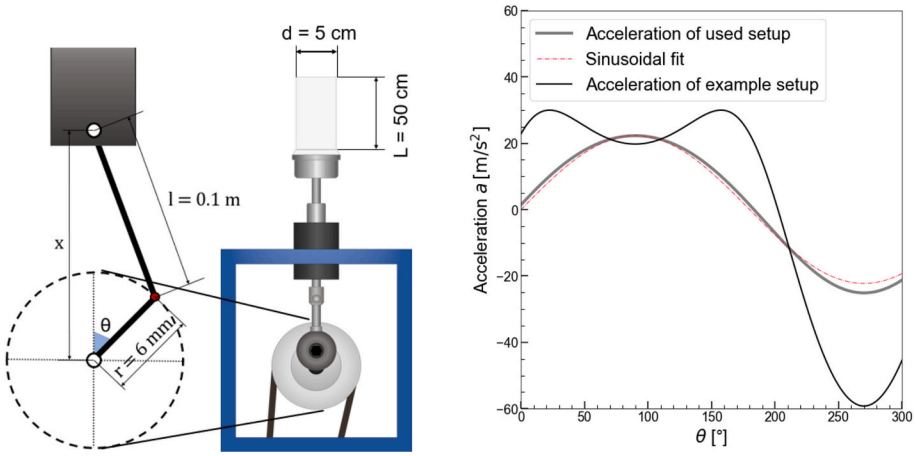

Fig. 1. Left: Sketch of the fluidized bed and its geometry showing the trigonometrical dependencies. Right: Acceleration over the angle θ of the piston for the used setup, an example setup and a sinusoidal function with the same amplitude as the used setup. Graphs were computed with a frequency of $f = 10$ *Hz*. The example setup had a crank length of 2 cm and an amplitude of 1 cm.

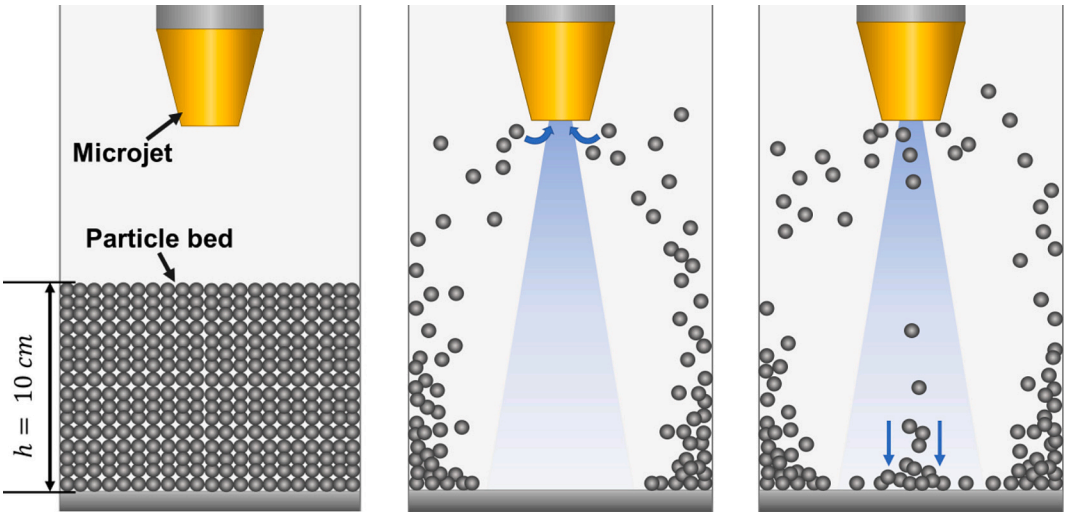

Fig. 2. 2D illustration of fluidized bed with secondary gas flow via a downwards micronozzle.

fluidized bed chamber. The pipe had an inner diameter of 6 mm and an outer diameter of 8 mm. A small micronozzle with a diameter r was attached to the tip of the pipe, pointing downwards vertically into the fluidized bed (Fig. 2). The secondary gas flow via jet is supplied with nitrogen from a pressured gas line to create high velocity flow at the outlet of the nozzle. It is assumed that the flow is choked and sonic, and that the Mach number is close to unity. Additionally, the flow is assumed to be adiabatic, frictionless, and compressible resulting in a nozzle velocity of 320 m/s [28].

3.2. Mixing experiments

For the ASSB cathode heteroagglomerate production, LFP (Life Power® P2 provided by Matthey Battery Materials GmbH, Germany), CB (C-NERGY SUPER C65 provided by IMERYS, France) and commercially available NaCl (Source Chemicals Ltd., UK) were mixed in a fluidized bed. LFP acts as the AM of the composite, while CB was added as the conductive additive. NaCl was used as a substitute material for characterizing the fluidization behavior in the fluidized bed and vibrated fluidized bed (FB/VFB) and in order to find optimal settings for fluidization in regards to composite mixing. In-house synthesized LIC (Battery LabFactory Braunschweig, Germany) was later used in 50 g batches to prepare electrochemically working ASSB cathodes, which were investigated after finding optimized parameters of the FB and VFB [12].

The raw materials were characterized in terms of particle size, raw, bulk and tap density, surface area and flowability. The surface area of the raw materials was determined via BET (Nova 4000e Surface Area Analyzer, Quantachrome Instruments, Boynton Beach, USA). The raw density was determined using a helium pycnometer (AccuPyyc 1330, Micromeritics, USA) while the bulk density and flowability were determined using a *FT4* powder rheometer (Freeman Technology Ltd., UK). The primary particle sizes $d_{50,3}$ below 1 µm were obtained via SEM, while the primary particle size of NaCl was obtained using the Camsizer XT on dry dispersion mode. An overview of different parameters regarding the particle properties, e.g., particle diameter, density, flowability and composite composition is in Table 1.

Table 1
Overview of particle properties.

	LFP sieved	NaCl	CB	LIC
Primary particle size $d_{50,3}[\mu m]$	0.8	9.22	0.04	<1
Raw density $\left[\frac{kg}{m^3}\right]$	3600	2200	2100	2590
Bulk density $\left[\frac{kg}{m^3}\right]$	354	300	82	910
Flowability ff_c [−]	5.27	1.85	1.98	2.49
BET Surface area $\left[\frac{m^2}{g}\right]$	12.10	4.55	85.3	3.46
Weight composition [%]	58	38	4	38

The flowability, in particular, has a decisive influence on the fluidity of fine powders and is therefore a crucial factor in the design of a fluidized bed system. Powders that have a flowability factor ff_c of 1 to 2 are considered very cohesive, between 2 and 4 as cohesive, while powders with a flowability of 4 and 10 are considered easy flowing [36]. While NaCl, LIC and CB are very cohesive, LFP is considered as easy flowing which was achieved through sieving of the particles using a mesh size of 180 µm (see Table 1). Compared to LIC, the NaCl has a lower flowability, indicating slightly higher cohesion between the particles, despite its significantly larger primary particle size. It should be noted that despite the primary particle size being smaller than the mesh size, the agglomerates may be well above 180 µm and will either fall through the sieve due to the motion during sieving, or will be filtered out.

3.3. Characterization methods

3.3.1. Electron microscopy

SEM images were acquired using an electron microscope (Zeiss Supra 55 VP, Zeiss company, Oberkochen, Germany). Further, we found that for the model material system an SE2 detector worked best, allowing to distinguish between particle species based on size, morphology, and contrast. Cross-sections were acquired for single agglomerates (FEI Helios Nanolab G3 UC, Thermo Fischer, USA). Regarding the battery material system containing LIC, the XEIA3 system (Xe-Plasma FIB, TESCAN GmbH, Germany) was used in combination with the transfer system Leica EM VCT500 (Leica Microsystems GmbH, Germany) to ensure consistent inert atmosphere due to the moisture sensitive nature of solid electrolytes, including LIC.

3.3.2. Electronic powder conductivity

The electronic powder conductivity was measured using a Zwick Z020 material tester (ZwickRoell GmbH & Co.Kg, Germany) that applies pressure through a plunger on the powder. The applied pressure results in compaction and improved contact between the particles that is dependent on the porosity. 1 g of cathode composite was compressed and a constant direct current of 10 mA was applied using a Digistant®4420 universal calibrator (Burster GmbH & Co KG, Germany). The voltage of the compressed cathode composite is constantly monitored and recorded. When a compression pressure of 70 kPa or 3 MPa is

reached and the resistance R calculated according to Ohms law. The conductivity σ_{spec} is then calculated from the thickness l of the compacted cathode composite and R and the cross-sectional area of the cylinder, described in Eq. (4). For more information on the measurement procedure please refer to the publication of Westphal et al. [37].

$$\sigma_{spec} = \frac{l}{R \bullet A} \tag{4}$$

3.3.3. Solid state battery cell assembly

Full solid state cell assembly was carried out inside an argon-filled glove box with impurity levels of $p(O_2)/p < 1.0$ ppm and $p(H_2O)/p < 1.0$ ppm. First, the separator was built by filling 35 mg of Li_6PS_5Cl (NEI corp., NJ, USA) in a cell chamber with a diameter of 10 mm and pressed with hand pressure. For the second layer of the separator, in-house synthesized LIC was filled into the cell and again tightened with hand pressure. Following that, 11 mg of the processed cathode mixture was evenly distributed on top of the LIC layer. The separator and the cathode mixture were then uniaxially compacted with a pressure of 380 MPa for 3 min.

A In/(InLi) anode was built by placing indium foil (100 μm thickness, 99.9999 %, chemPUR, Germany) with a diameter of 9 mm on top of lithium foil (100 μm thickness, 99.9 %, China Energy Lithium, China) with a diameter of 6 mm on the opposite side of the cell. The cell was fixed in a steel frame consisting of 4 symmetrical screws and threaded rods that were each tightened with 4 Nm of torque for 30 min to enable the diffusion of the In/Li with a stable potential of 0.62 V vs Li^+/Li. Then, the cell was tightened with 10 Nm of torque which leads to a pressure of about 60–80 MPa. Finally, the cell was cycled at 0.1 C for 10 cycles between 1.9 V and 3.4 V vs In/InLi.

3.3.4. Particle and agglomerate size measurement

All particle or agglomerate size distributions with the exception of the primary particle size were measured in dry mode using no dispersion pressure to maintain the agglomerate size and morphology (Camsizer XT, Retsch GmbH, Germany). During the measurement, the agglomerates fall through a chamber where their size is recorded via dynamic image analysis.

4. Results and discussion

4.1. Fluidization of raw materials

The fluidization behavior of the raw materials LFP, CB, and NaCl (later also LIC) was investigated to establish strategies for enabling and optimizing the fluidization of these powders. In this process, the vibration and the change of its frequency, as well as the particles' pretreatment through sieving or drying were explored. The bed pressure drop was recorded, starting with a high superficial gas velocity. The initial bed height of a single particle species was set constant to $h = 10$ cm.

The bed pressure drop $\Delta p_{measured}$ was measured between the bottom of the bed and the exhaust of the fluidisation chamber, disregarding the distributor plate for the pressure drop. To evaluate the quality of the fluidization, the normalized bed pressure drop $\Delta p_{normalized}$ was used and calculated according to Eq. (5). Here, Δp_{weight} is the theoretical bed pressure drop, which is described by the mass of the particle bed m, the earth acceleration g and the cross-sectional area A.

$$\Delta p_{normalized} = \frac{\Delta p_{measured}}{\Delta p_{weight}} = \frac{\Delta p_{measured}}{\frac{m \bullet g}{A}} \bullet 100\% \tag{5}$$

In fluidized beds, the bed pressure drop usually increases with superficial gas velocity. In case of full fluidization, $\Delta p_{measured}$ divided by Δp_{weight} is close to 1, as the weight is held by the fluidization gas, which is expressed through a measurable pressure drop.

For full fluidization, there are two ways to determine the minimum fluidization velocity. One is to extrapolate the linear relationship between the gas velocity and the corresponding weighted bed pressure drop Δp_{weight} at low gas velocities. The point at where the linear function intersects with the maximum bed pressure drop, is then identified. This intersection corresponds to the gas velocity, which defines the minimal fluidization velocity. The other method, that is often used in literature regarding nanofluidization and also in this contribution, is to extract the minimum gas velocity, at which the normalized pressure drop becomes independent of the gas velocity. Additionally, the bed pressure drop remains at the plateau level at velocities lower than those needed to attain fluidization [26].

4.1.1. Fluidization without vibration

The fluidization of CB as well as NaCl was challenging due to channelling and plug flow and segregation effects which hindered full fluidization of the bed. Both materials failed to achieve full fluidization, even after sieving larger particles and agglomerate clusters. This could be caused by the highly cohesive behavior of NaCl and CB with low flowability factors (see Table 1). They are caused by high adhesive forces acting between the particles, holding the powder bed together and complicating smooth fluidization without channelling or plug flow behavior.

However, LFP showed proper fluidizability for all three investigated pretreatment cases without the application of an additional vibration. The three cases are: untreated LFP, dried LFP, and sieved LFP (Fig. 3). Sieving with an analytical sieve with a mesh size of 180 μm led to a removal of larger agglomerates for LFP, resulting in a lower minimum fluidization velocity.

As seen for LFP (Fig. 3A), the normalized pressure drop $\Delta p_{normalized}$ reaches a plateau for LFP, regardless of the pretreatment. Although a normalized bed pressure drop of 100 % was not achieved, it can be assumed that the entire bed could be completely fluidized due to the independence of the pressure drop from the surface gas velocity. The measurement in this setup may not cover the entire bed, which is caused by the placement of the lower pressure tap, which is located slightly above the distributor plate and therefore may not capture the full pressure drop of the bed. It follows that $\Delta p_{normalized}$ depends on the bed height. For this reason, in following bed pressure drop measurements the maximum bed pressure drop is normalized to 100 %. However, it should be noted that a measurement below the sintered steel plate was not feasible during operation, as small particles keep entering the pores of the distributor plate. This results in a pressure drop change of the distributor plate during operation that cannot be subtracted from the total pressure drop.

The minimum fluidization velocities of the LFP are lowest for the sieved LFP ($u_{mf} \approx 5.32 \frac{cm}{s}$) and highest for the untreated LFP, that was stored at normal conditions ($u_{mf} \approx 9.55 \frac{cm}{s}$). Drying but not sieving the LFP leads to a slightly decreased minimum fluidization velocity ($u_{mf} \approx 7.42 \frac{cm}{s}$) due to the reduced capillary forces. The fluidization velocity is strongly influenced by the particle or agglomerate size of the materials, which again is dependent on the interparticular forces, which are dependent on the particle properties and storing conditions. Comparing the agglomerate size distribution of untreated LFP and sieved LFP (Fig. 3B), the number of larger agglomerates, decreased when LFP is sieved. This reduction in particle size leads to an improved fluidizability with decreased u_{mf}, as large firm agglomerates and clumps have been removed or crushed to a smaller size, even if the size reduction may only be temporary. After the sieving process, larger agglomerates above 1 mm were still present. These relatively large agglomerates may not be as firm after sieving, leading to breakage of large agglomerates during fluidization, causing an initial decrease of agglomerate size during fluidization. The loss of agglomerate strength through sieving can be attributed to the fact that all agglomerates had to be smaller than the sieve's mesh to pass through. The physical stress of passing through the mesh likely contributes to the breakage of these

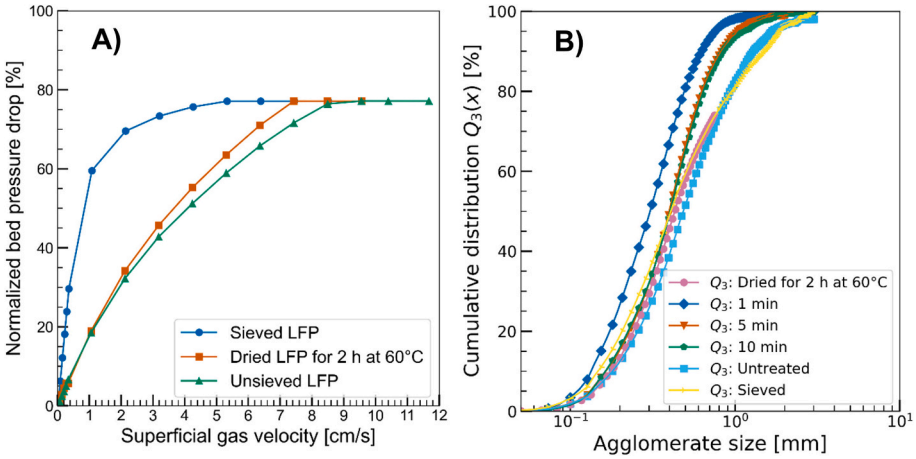

Fig. 3. A): Normalized bed pressure drop curve of sieved LFP without vibration and different treatment. No vibration or other assistance methods were applied. B): Agglomerate size distributions Q_3 of LFP for different fluidization times and pre-treatments before fluidization.

larger, weaker agglomerates. During fluidization, an increase in agglomerate size was observed. The agglomerate size distribution did not differ between 5 min and 10 min of fluidization, indicating an equilibrium between deagglomerating and agglomerating forces.

Overall, sieving improved unassisted fluidization and decreased the mean agglomerate size. This improvement suggests that sieving not only removes larger agglomerates and breaks, less stable agglomerates. Consequently, this leads to more efficient fluidization due to the presence of smaller and more uniformly sized agglomerates. An overview of the agglomerate sizes is given in Table 2.

When sieved LFP was fluidized for 1 min, the agglomerate size was reduced significantly and became narrower, as large agglomerates broke down during fluidization (see Fig. 3B). A possible explanation for this observation is, that LFP agglomerates continuously experience shear forces during fluidization due to constantly colliding with other agglomerates or the wall. Therefore, the agglomerate size is a result of all acting forces that cause shearing and breakage of the agglomerates.

During fluidization, submicron sized and nanoparticles fluidize as agglomerates due to the interparticular forces which can be of several hundred micrometres large. However, it should be kept in mind that the fluidization of submicron sized particles and nanoparticles is a dynamic process, in which primary particles are dynamically exchanged between agglomerates [29]. This means that agglomerates change their shape and number of primary particles during fluidization [38]. It follows that any kind of measurement that is done offline may have a slightly different result in regards to agglomerate size and shape due to transport effects or particles adsorbing moisture from the atmosphere [29,38].

4.1.2. Fluidization with vibration

The effect of vibration on the fluidization behavior was investigated by adding vibration to the system, which adds an additional force to the process. The vibration can be characterized through the vibration intensity Λ, which is comprised of the amplitude A and the frequency f and the gravitational acceleration g described in Eq. (6). It describes the maximum acceleration caused by the vibration in relation to the gravitational acceleration.

$$\Lambda = \frac{A \bullet 2\pi \bullet f^2}{g} \tag{6}$$

In this contribution, only the effect of the frequency f is evaluated as the amplitude kept constant at 6 mm.

By applying a vibration frequency of 8.8 Hz, NaCl and CB, along with LFP, were successfully fluidized. At higher frequencies beyond 8.8 Hz, the fluidization process was enhanced, resulting in slight increased bed expansion. However, the bed expansion is not further elaborated upon here, as the primary objective is to demonstrate the feasibility of fluidizing and mixing battery materials.

4.1.3. Dry room fluidization

Dry room processing is a necessary requirement for the handling of many battery materials especially solid electrolytes for ASSBs, due to their moisture sensitive nature [39]. In this work, the fluidization behavior of the halide solid electrolyte LIC was investigated. The minimal fluidization velocity of dry (vacuum dried at 60 °C for at least 48 h) LFP, CB and LIC was evaluated for 6.6 Hz, 8.8 Hz, and 11 Hz.

Using a vibration frequency of $f = 8.8$ Hz all materials could be fluidized. This was also the case for 11 Hz and mostly 6.6 Hz. However, for CB, no minimal fluidization velocity could be determined at the lowest investigated frequency of 6.6 Hz in the investigated flow range of $u = 10$ cm/s. LFP has the overall lowest minimal fluidization velocity, followed by NaCl, LIC and CB whereas the minimal fluidization velocity decreased with increasing vibrational frequency. An overview of the minimal fluidization velocities u_{mf} is shown in Table 3.

It should be noted, that the determination of the minimal fluidization velocity is not entirely precise when vibration is applied. Vibration induced pressure fluctuations occur, that are of large amplitude compared with the actual recorded signal. All pressure measurements were done by averaging the electrical signal with a measurement frequency of 2500 Hz. However, there is still some leftover noise that could not be avoided. The resulting minimal fluidization velocity is accurate enough to read, but the result only serves as an estimate. Overall, the minimal fluidization velocity decreases with increasing vibration intensity Λ (see Table 3). Some values are the same as only certain volume flow rates were applied. As such, the flow rate and the corresponding superficial gas velocity where the pressure becomes independent may fall into the same range. For LFP, sieving leads to higher u_{mf} compared to vacuum dried unsieved LFP, while the opposite is true for CB. Sieving can break down larger agglomerates into smaller, more uniform agglomerates thereby improving fluidization but can also potentially create more porous structures. This may decrease the apparent density

Table 2
Overview of particle sizes for different states of LFP.

LFP	$d_{10,3}$ [mm]	$d_{50,3}$ [mm]	$d_{90,3}$ [mm]
Fluidized 1 min	0.269	0.305	0.626
Fluidized 5 min	0.164	0.398	0.822
Fluidized 10 min	0.163	0.403	0.840
Untreated LFP	0.180	0.486	1.280
Sieved LFP (180 µm)	0.147	0.407	1.495
Dried for 2 h at 60 °C	0.176	0.432	1.152

Table 3
Overview of all measured minimal fluidization velocities for normal and vacuum dried conditions as well as differently pre-treated material.

LFP (sieved)			LFP (vacuum dried)		
f [Hz]	Λ [−]	u_{mf} $\left[\frac{cm}{s}\right]$	f [Hz]	Λ [−]	u_{mf} $\left[\frac{cm}{s}\right]$
6.6	1.05	5.32	6.6	1.05	3.18
8.8	1.86	3.18	8.8	1.86	1.58
11	2.92	0.70	11	2.92	0.19

CB (sieved)			CB (vacuum dried)		
f [Hz]	Λ [−]	u_{mf} $\left[\frac{cm}{s}\right]$	f [Hz]	Λ [−]	u_{mf} $\left[\frac{cm}{s}\right]$
6.6	1.05	–	6.6	1.05	–
8.8	1.86	1.05	8.8	1.86	5.98
11	2.92	1.05	11	2.92	5.30

NaCl (sieved)			LIC (vacuum dried)		
f [Hz]	Λ [−]	u_{mf} $\left[\frac{cm}{s}\right]$	f [Hz]	Λ [−]	u_{mf} $\left[\frac{cm}{s}\right]$
6.6	1.05	1.05	6.6	1.05	3.71
8.8	1.86	0.65	8.8	1.86	2.64
11	2.92	0.34	11	2.92	1.59

of the agglomerates and thus their u_{mf}. As for vacuum drying, it leads to more denser particles with less porosity, increasing u_{mf} in case of CB. When sieving was applied to CB, it led to the breakage of very large agglomerates, therefore decreasing u_{mf}. Contrary, for the vacuum dried CB large agglomerates were still present, leading to a higher u_{mf}. Overall, both sieving and drying improved the fluidization behavior of the materials.

In order to evaluate the effect of vibration on the powders, the normalized fluidization velocity is shown in Fig. 4. It was calculated by dividing the u_{mf} at the given vibration intensity by the determined u_{mf} at the lowest measured vibration frequency, which was 6.6 Hz for LFP, NaCl and LIC and 8.8 Hz for CB and multiplying by 100 %.

While LFP, LIC and sieved NaCl could be fluidized at a frequency of $f = 6.6\,Hz - 11$ Hz which corresponds to $\Lambda = 1.09 - 2.92$, CB could only be fluidized using a frequency of 8.8 Hz and 11 Hz, which is why in Fig. 4 only two datapoints are shown for CB. At lower frequencies channelling occurred and not the whole bed could be agitated. Nevertheless, using vibration was most effective on LFP, as the minimal fluidization velocity decreased below 10 % of the minimal fluidization velocity at $\Lambda = 2.92$ compared to $\Lambda = 1.09$. Overall, in the observed range of used frequencies the vibration decreased the minimal fluidization velocity for all materials except for carbon black, where the value only decreased marginally. Arguably, an increase of the vibration intensity would likely incur a further decrease of the minimal fluidization velocity. Nonetheless, vibration enabled the fluidization of carbon black, which is essential for the movement and therefore the mixing in a fluidized bed.

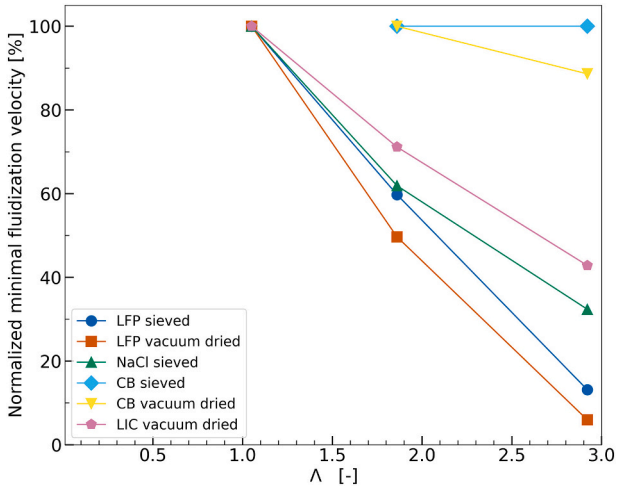

Fig. 4. Minimal fluidization velocities LFP, CB, NaCl and LIC for different vibrational frequencies and pretreatment.

4.1.4. *Fluidization of the LFP – NaCl – CB material system*

4.1.4.1. Visual examination of mixing behavior with vibration and without jet assistance. The mixing of the model material system including NaCl, is investigated to evaluate the mixing and agglomeration behavior and to identify optimal parameters for the model battery material system. The material system that is evaluated consists of 58 % wt% LFP, 38 % wt % NaCl and 4 % wt% CB. The initial bed height was set to 10 cm. Fluidization was done with a vibration frequency of 11 Hz and superficial gas velocity was set to 9 cm/s to ensure full fluidization, based on the previous results with the raw materials. The surface of the agglomerates was observed using an SEM at different processing times.

Fig. 5A–C depict surfaces of agglomerated composites that were processed for different fluidization times. The particles were distinguished by morphology and size of the primary particles and color-coded according to its material identity based on the particle morphology of the primary particles. The surface of all agglomerates contains all types of primary particles in a single agglomerate, confirming the successful production of heteroagglomerates in a fluidized bed.

As mixing time increases, the distribution of the primary particles becomes more uniform. CB becomes more distributed and smaller CB clusters appear with increasing fluidization time, speaking for an overall improvement of the macroscopic mixing behavior. At the same time the change of cluster size indicate that the clusters are constantly breaking and agglomerating with other clusters.

However, a quantitative investigation of the mixing degree was not conducted, as the SEM only looks at the surface of the agglomerates. In case of heteroagglomerates consisting of LFP, CB, and NaCl, the structure should be isotropic, so that a quantitative evaluation of a mixing

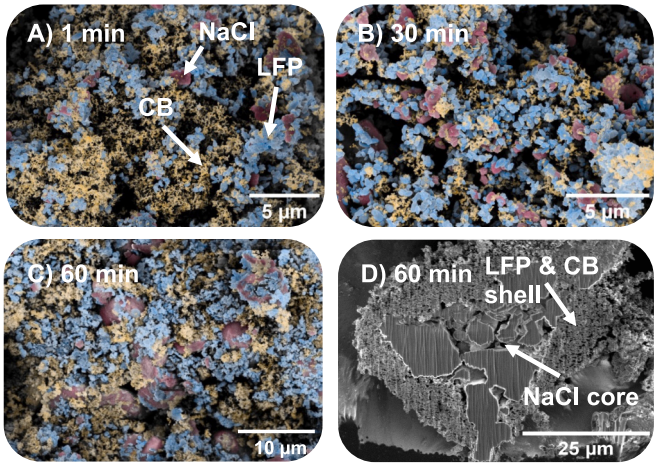

Fig. 5. False colour images acquired by SEM at 10 kV and an SE2 detector with subsequent segmentation. Processing times A): 1 min, B) 30 min, C) 60 min. The surface of single agglomerates that consist of LFP (blue), CB (yellow) and NaCl (red). D) shows the FIB cross section of an agglomerate with an LFP-CB shell and NaCl core. Processing time was 60 min. (For interpretation of the references to colour in this figure legend, the reader is referred to the web version of this article.)

can be statistically meaningful. For this reason, the consideration of the surface alone is insufficient to determine whether all particle species are distributed throughout the agglomerates.

To gain more insight into the agglomerate structure, FIB cross sections were taken (see Fig. 5D). Investigating the cross section of a single agglomerate fluidized for 60 min, it is revealed that the mixing is inhomogeneous within the heteroagglomerates. The heteroagglomerate core consists of NaCl, while the shell consists of a mixture of LFP and CB nanoparticles. Although a single agglomerate may not fully represent the entire process, this finding indicates that some agglomerates fail to achieve homogeneous distribution of the materials. While there is evidence of macroscopic mixing of the materials on the surface, shown through SEM imaging, the FIB cross sections show that heteroagglomerates predominantly remain unmixed on a microscale.

From these findings, it can be concluded that the scale of breakages occurring during fluidization is insufficient to completely disintegrate agglomerates and especially large NaCl clusters remain. Instead, the surface of the agglomerated mixture continuously exchanges small primary particles and smaller clusters with other agglomerates. In general, whether agglomerates will break during fluidization depends on various parameters, such as collision forces, interparticular forces, and particle characteristics including species and shape. In the case of the LFP-NaCl-CB system, the interparticular forces within NaCl agglomerates are too strong to be broken by fluidization.

4.1.4.2. Electronic powder conductivity of mixed powder without jet assistance. The electronic powder conductivity can serve as a macroscopic indicator of the microstructural characteristics of the electronically conductive materials CB ($6760\frac{\mathrm{mS}}{\mathrm{cm}}$) and LFP ($12.3\frac{\mathrm{mS}}{\mathrm{cm}}$) and electronically isolating NaCl or LIC particles, respectively [40]. The electronic powder conductivity was evaluated three times for different processing times to ascertain whether fluidization induces alterations in the microstructure and affects the percolation of the CB and LFP within the cathode composite (see Fig. 6).

The electronic powder conductivity decreases with increasing fluidization time but quickly reaches a plateau, suggesting that the microstructure influenced conductivity remains relatively stable after initial structural changes. The initial decrease in conductivity may result from the breakage of very large CB agglomerates and the breakage of lose NaCl that has an insulating effect. Given the stability of the electronic powder conductivity over extended fluidization times (60 min), it can be inferred that the extent of long-range contact among CB that cause the electronic conductivity chains remains unchanged. However, visual observation (see Fig. 5) revealed that the structure and distribution of CB evolves with increasing fluidization time, even after 30 min of fluidization. If submicron sized particles are continuously exchanged and the microstructure is consistently changing, this would be reflected in the electronic powder conductivity. However, since the powder conductivity remains constant (see Fig. 6), it can be hypothesized that long-range percolation responsible for electronic conductivity is not further inhibited by relatively large NaCl agglomerates which are electronically non-conductive. At the same time the electronic conductivity is not improved by the overall improved distribution of the LFP and CB at the surface of the agglomerates.

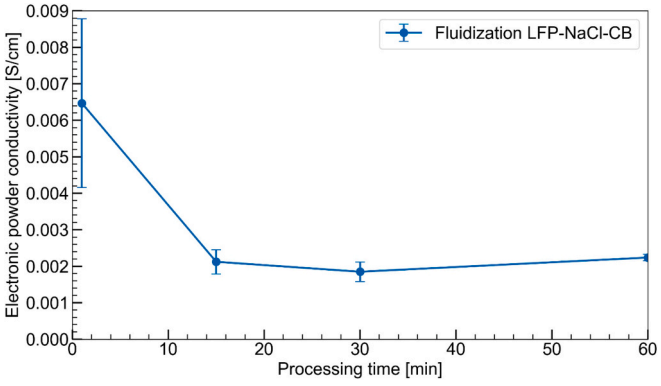

Fig. 6. Evolution of the electronic powder conductivity of the LFP-NaCl-CB material system in a vibrated fluidized bed measured at 70 kPa.

4.2. Experimental study on jet assisted fluidization

Fluidizing NaCl (and LIC), LFP and CB revealed only macroscopic mixing with large NaCl clusters still present in the heteroagglomerates. These larger clusters would lead to difficulties in an ASSB electrochemical performance due to the lack of ionic pathways and insufficient connections of the AM particles. Thus, additional forces are necessary to break up these large NaCl (or LIC) agglomerates and thus increase the number of heterocontacts between LFP – CB – NaCl (later LIC).

Additional forces were added by jet assistance at fluidization and a vibration intensity of $\Lambda = 1.51$ ($f = 7.92$ Hz, $A = 6$ mm). The superficial gas velocity resulting from the primary gas flow was set to 4.2 cm/s. The secondary gas flow increases the superficial gas velocity and is dependent on the nozzle size and the resulting velocity. A nozzle with an opening size of 1 mm with a distance of 1 cm to the distributor plate was installed. The resulting secondary gas flow from the nozzle results in an increase of the overall superficial gas velocity of 12.7 cm/s, adding up to a total of 15.7 cm/s considering the velocity of the fluidization gas. It was evaluated whether a secondary jet would be able to produce and improve the mixing or change the microstructure of battery heteroagglomerates.

4.2.1. Visual observation of produced mixture with jet assistance

SEM images and cross-sections of random agglomerates and pressed composite materials were analysed, including a larger field of view cross-section and surface examination of an exemplary agglomerate (Fig. 7).

Qualitatively, the surface of the pressed composite appears to be mixed as well with nanoparticles similar to the VFB sample that was fluidized for 60 min (Fig. 7C). The cross section in Fig. 7A) shows that jet assisted fluidization led to a good distribution of the CB, NaCl and LFP throughout the agglomerate. The cross-section of a larger area of the LFP-CB-NaCl sample mixed with jet assistance (Fig. 7B) indicates that the NaCl agglomerates have been deagglomerated during the process, becoming loose and unconnected within the composite. This was consistent across all observed cross-sections. The core-shell structure

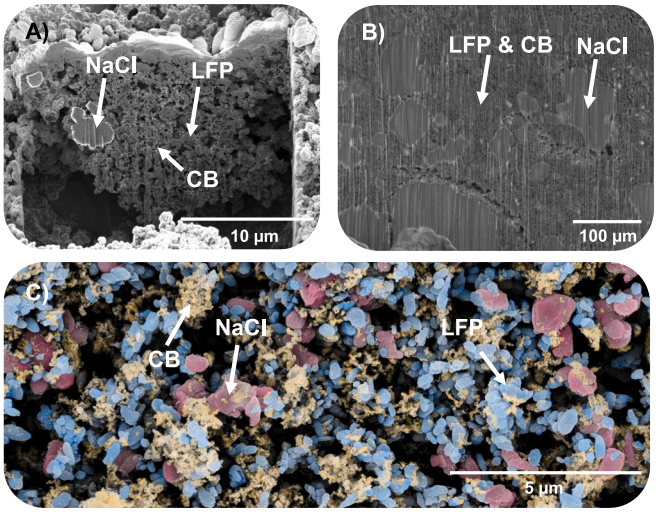

Fig. 7. A) FIB-SEM cross section of the agglomerate. B) FIB-SEM cross-section with a larger field of view. C) Surface of an agglomerate. Composite was processed with a microjet for 1 min using a 1 mm nozzle with 1 cm height.

observed during fluidization alone was no longer present when the jet was applied. Thus, the use of a secondary microjet improved the mixing and dispersion capabilities of the fluidized bed significantly. By applying a high velocity microjet, mixing on a microstructural level below a few micrometres was achieved, which was not the case with only fluidization.

The application of a jet with high gas velocity may suffer from large amounts of elutriation of material due to the increased volumetric flow. When the process is upscaled, it is not yet clear how many jets in which configuration are required to achieve similar results and further studies have to be conducted to investigate this question. Copious parameters may be adjusted, such as reactor diameter, nozzle size, positioning, jet gas, distance to the distributor plate, number of jets. Further, it is not clear what kind of deagglomeration mechanism is underlying when using a secondary gas flow through a microjet. Whether agglomerates collide with each other, or with the walls, e.g. the distributor plate, or are sheared by the gas jet is not yet clear and beyond the scope of this work.

4.2.2. *Electrical powder conductivity of mixed powder with jet assistance*

Deagglomeration of CB, NaCl, and LFP agglomerates can lead to strong changes in the electronic powder conductivity. This deagglomeration and subsequent heteroagglomeration is strongly influenced by jet assistance which induces larger shear and normal forces on the materials. As jet assistance with larger nozzle sizes lead to heavy elutriation, a smaller nozzle diameter of 0.2 mm was chosen.

Despite the superficial velocity being about the same as with only fluidization gas (no jet assistance), the elutriation of the particles at similar superficial gas velocities was significantly higher due to smaller particle sizes that are present when a microjet is applied. For this reason, the operation time was limited to 1 min so that enough sample could be retrieved for subsequent analysis.

Here, the influence of the nozzle diameter on the bulk density and electronic powder conductivity is evaluated (see Fig. 8). Examination of the influence of distance to the distributor plate to the jet shows and increasing bulk density of the fluidized mix with decreasing distance with a nozzle size of 6 mm (see Fig. 8). With decreasing distance to the distributor plate, the agglomerates appear to be subjected to higher levels of stress for a nozzle size of 0.2 mm, resulting in smaller agglomerates and thus, a higher packing density during electronic powder conductivity measurement is obtained. At the same time, the electronic powder conductivity decreases with increasing jet height before increasing again at a distance of 10 cm for the nozzle sizes of 0.4 mm and 0.6 mm. At this distance, the bulk density is the lowest, and NaCl, which is electronically isolating, may not be deagglomerated as much due to the lower stress acting on the NaCl agglomerates at this height. Thus, the relatively high electronic conductivity is caused by a small amount of electronically isolating particles. With decreasing nozzle distance, NaCl is increasingly deagglomerated leading to an increase in the isolating particle number and thus a decrease in powder conductivity. In contrast, CB which possesses a high electronic conductivity is deagglomerated at all nozzle heights resulting in a large amount of electronically conductive particles. This leads to an increase in bulk density and an increasing amount of short-range electronic pathways and thus an increase in electronic powder conductivity. These results are in good agreement with the electronic powder conductivity measurements for conventional LIB powder composites containing NCM and CB [41,42].

Conclusively, two counteracting effects must be considered: The dispersing of CB agglomerates leading to an increase in electronic powder conductivity by an increase in short-range electrical contacts, increase of particle contacts due to increase in bulk density, and homogenization of the CB within the composite. At the same time NaCl acts as an insulator that mimics the behavior of solid electrolytes and hinders the conduction paths of the CB, counteracting the improvement in powder conductivity caused by the distribution of the CB. At higher nozzle heights, the NaCl agglomerates are less likely to be broken down, allowing the CB to coat NaCl agglomerates, thereby increasing the electronic conductivity without NaCl hindering the conduction paths.

The electronic powder conductivity for 0.2 mm is the smallest, while at larger nozzle sizes there's a significant increase of the electronic powder conductivity. With changing nozzle diameter and constant exit velocity of the microjet, the hydrodynamics of the fluidized bed change due to an increase of volume flow at larger diameters. It follows that particles that may be entrained at one nozzle diameter will cause collisions for some particles of certain size while at other nozzle diameters this may not be the case. It should be mentioned that the superficial gas velocity at larger nozzle diameters is significantly higher and quadruples between 0.2 mm and 0.4 mm nozzle size, while the 0.6 mm nozzle size has a 9 times increase in superficial gas velocity stemming from the secondary gas flow (see Table 4). The resulting superficial gas velocities are shown in Table 4. For instance, the bulk density development reveals that at a diameter of 0.6 mm, the agglomerates experience significantly more shearing at higher nozzle heights, as indicated by the increase in bulk density (see Fig. 8). However, the electronic powder conductivity rises between 0.5 cm and 5 cm nozzle height, but drops again at a 10 cm nozzle height, which is also the case for 0.4 mm nozzle diameter. It appears that at these nozzle diameters, the electronic conductivity of the powder initially increases due to improved homogenization or increased bulk density, but then decreases as the carbon black (CB) chains break apart from excessive deagglomeration, despite the continued increase in

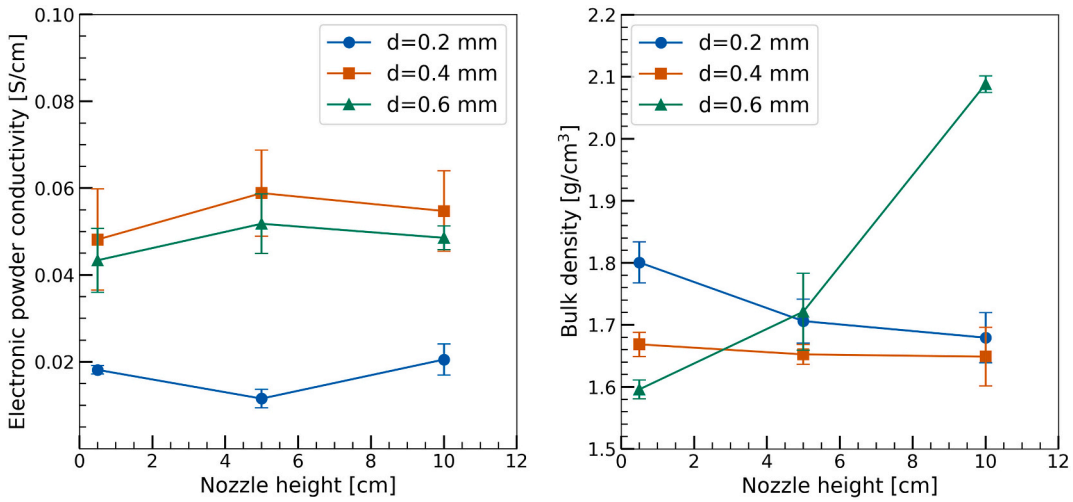

Fig. 8. Bulk density and electronic powder conductivity and at 3 MPa for different nozzle diameters. Powder was processed for 1 min.

Table 4
Superficial gas velocities for different nozzle diameters with a velocity of 320 m/s.

Nozzle diameter [mm]	Fluidization gas velocity [cm/s]	Nozzle volume flow $[cm^3/s]$	Δ Superficial gas velocity [cm/s]	Total superficial gas velocity
0.2	4.2	10	0.51	4.72
0.4	4.2	40	2.05	6.25
0.6	4.2	90	4.61	8.81

bulk density. At 0.4 mm the bulk density does not change significantly, while at 0.2 mm nozzle diameter the bulk density decreases with increasing nozzle height. Contrary, at 0.6 mm the bulk density increases with increasing nozzle height and shows the highest shear forces. As there is no clear trend in terms of shearing intensity with changing nozzle diameter, it could mean that the change of the hydrodynamics may be the cause for the differences on the overall amount of shearing, but this will require further investigations. However, it can be argued that the deagglomeration is dependent on the velocity gradient at the outlet of the jet, and the circumferential area, as they may determine the intensity (velocity gradients) and frequency of collisions (circumferential area). As the nozzle diameter increases, the velocity gradient becomes smaller, but the number of collisions increase as more particles are accelerated by the jet.

One issue that should be addressed here is the elutriation of particles. The jet introduces forces through collisions and velocity gradients, acting like a mill, which can be observed by the increasing bulk density of the powder mixture. The minimal fluidization velocity presented in chapter 5.1.1 is only valid if no jet is applied, as the agglomerate size remains relatively constant. It was observed that as the jet introduces forces that break agglomerates in the fluidized bed, the amount of elutriation and therefore material loss increased as well. This effect is further enhanced with larger nozzle sizes, as the grinding of the agglomerates leads to even smaller particles with a lower minimal fluidization velocity. Regarding this contribution, the elutriation and the CB content were not quantified, possibly skewing the results of the electronic powder conductivity, especially at higher superficial gas velocities. The control of elutriation and hydrodynamics is necessary to manage the process more precisely but will be part of future investigations.

4.3. Investigation of LIC – CB – LFP system

Previous results have shown that with a vibration intensity of $\Gamma = 1.51$ and using a jet with a nozzle diameter of 0.6 mm, the best bulk density of LFP, CB and NaCl is achieved. Though, using a jet with a nozzle diameter of 0.6 mm, large amounts of elutriation occur. Thus, for the fluidization of the ASSB mix consisting of LIC, LFP, and CB, a nozzle diameter of 0.4 mm with a nozzle height of 0.5 cm was chosen for the investigation of the LIC-CB-LFP material system, as it is the best compromise between the bulk density and elutriation. Fig. 9A) shows that after fluidization without a jet, large spherical agglomerates of several micrometres are present. This is congruent with the observation from the experiments on fluidization of pure LFP-NaCl-CB material system and is caused by the high interparticular adhesive forces of small agglomerates that are not broken during processing. For the LFP-NaCl-CB material system the particles were not as spherical compared to the LFP-LIC-CB material system, due to the large particle size of the NaCl. However, during fluidization, nanoparticles are exchanged on the surface leading to spherical particles for the material system including LIC and coated, less spherical agglomerates for NaCl due to homogeneous stress across the agglomerates.

In comparison, looking at the fluidized mixture with jet assistance (Fig. 9B) less spherical agglomerates are visible, which is based on the high shear forces of the jet and during impact which cause the subsequent deagglomeration of LFP, CB, and LIC homoagglomerates.

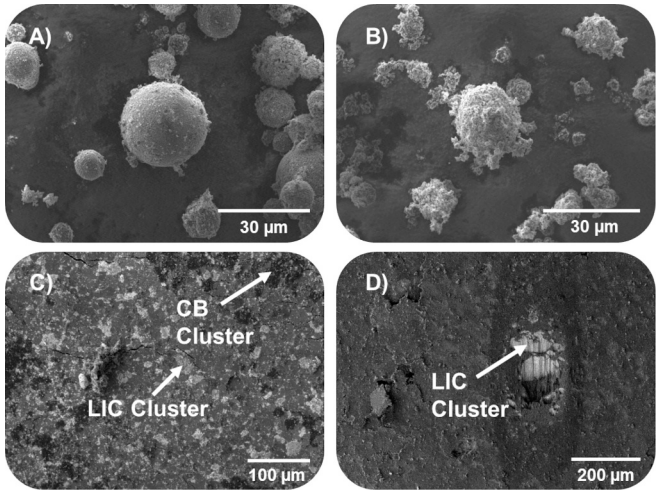

Fig. 9. Produced LIC-CB-LFP mix. A) SEM image of an agglomerate after fluidization for $t_{fl} = 60$ min. B) SEM image of an agglomerate after applying a nitrogen jet for 1 min. C) Top view of compressed composite section for fluidization for $t_{fl} = 60$ min. D) FIB-cross section of nitrogen jet application for 1 min.

In addition, coarser clusters adhering to the LFP can be seen, which presumably consist of large LIC or CB agglomerates. This observation suggests that macroscopic mixing of agglomerates has occurred, but that sufficient homogeneity has not been achieved at the submicron level. Large LFP agglomerates and LIC clusters would ensure that the LFP is largely ionically unbound, which would have a negative impact on the performance of the ASSB.

With applying a nitrogen jet no pure LFP spheres are present, but non-round heteroagglomerates were formed consisting of LFP, CB and LIC (Fig. 9B). This should have a positive effect on the electrochemical performance of the cell prepared from this mixture, as the LFP could be better ionically bonded with the solid electrolyte leading to ionic pathways in the ASSB cathode.

Without the use of a nitrogen jet, only macroscopic mixing takes place, which was clearly evident from visible coarser CB and LIC agglomerates. Mixing and the degree of comminuted LIC, LFP and CB agglomerates is reflected in the electronic conductivity of the prepared composites (Fig. 10). For the mixture prepared after $t_{fl} = 60$ min without a jet, a relatively high electrical conductivity with a large standard deviation can be seen. The high electronic conductivity indicates that coarse CB and large LIC clusters are present in the composite, leading to a high electronic conductivity. In addition, the high standard deviation of the VFB processed composite suggests that there is insufficient macroscopic homogeneity in the composite. As previously iterated in chapter 5.1.1, the forces within the VFB were insufficient to break larger NaCl clusters and were also insufficient to cause agglomerate breakage and deagglomeration of LIC. In Fig. 9C), clusters of CB and LIC can be seen, which is attributed to the inability of the VFB to break larger agglomerates but were also mixed to on a scale that is comparable to the agglomerate size.

For the mixture prepared with a nitrogen jet, a lower electronic powder conductivity with a small standard deviation is observed. This indicates a more homogeneous mixing of the sample, whereas the low electronic conductivity hints that coarse CB, LIC and LFP agglomerates have been broken up and a homogeneous mixture was formed. The decrease in electronic conductivity can be explained by the deagglomeration of insulating LIC agglomerates, which act as electron blockers in the composite, which was also observed by Frankenberg et al. [12].

The homogeneous distribution of LIC, CB and LFP particles as well as

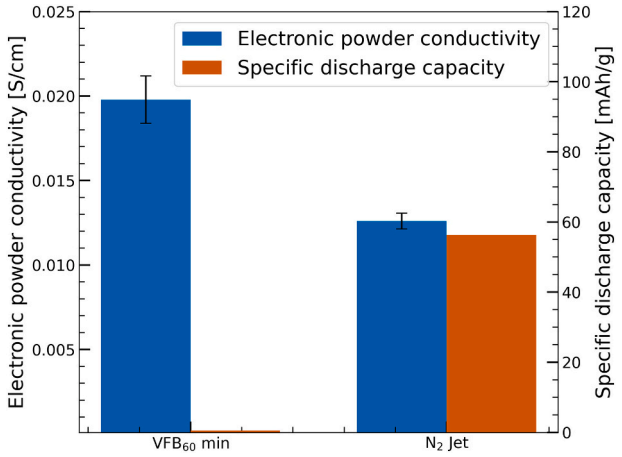

Fig. 10. Electronic powder conductivity and specific discharge capacity of LIC-CB-LFP samples with and without application of a nitrogen jet.

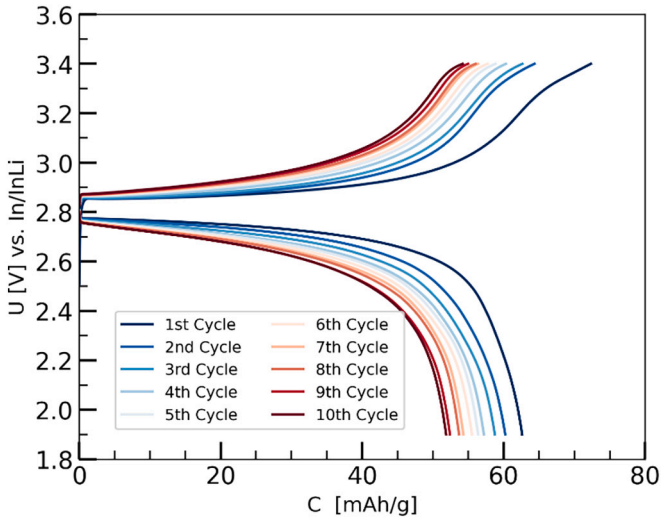

Fig. 11. Charge-discharge curve of the LIC-CB-LFP sample with the application of a nitrogen jet.

comminution of LIC, CB and LFP agglomerates and heteroaggregation of these 3 materials when a nitrogen jet is applied, is expected to lead to an enhanced performance of the ASSB cell. This was investigated by cycling the prepared composites for ten cycles and evaluating the mean specific discharge capacity $C_{\text{discharge}}$ (see Fig. 11).

The cyclization results of the cells prepared from the mixture by a VFB after $t_{\text{fl}} = 60$ min without a jet, reveal that only a fraction of the theoretical capacity of LFP ($C_{\text{discharge,LFP}} \approx 140$ mAh/g) is achieved. With about 0.5 mAh/g, $C_{discharge}$ is far below the theoretically achievable capacity. This is due to insufficient homogenization in the form of large CB and LIC agglomerates, as well as agglomeration of LFP in the fluidized bed. Almost all of LFP particles are ionically unbound and thus cannot act as cathode active material in the cathode network during charging and discharging.

With jet assistance an enhanced AM utilization is reached, which is displayed in an increased discharge capacity of about 56 mAh/g. Thus, the use of a jet and the application of high normal, and shear forces are necessary to generate heteroagglomerates consisting of LFP, CB and LIC and to break up coarse agglomerates of LFP, LIC and CB that are present without jet application. However, the theoretical capacity of LFP is not reached, indicating that there is still a substantial amount of LFP that is ionically unbonded. To further increase the AM utilization, in future the VFB design will be improved and the process will be optimized. However, this study shows that in principle it is possible to process ASSB cathode composites within an VFB.

5. Conclusion and outlook

In this work, the proof of concept for processing solid-state battery materials in a vibrated fluidized bed using a high-velocity microjet is presented. First, the fluidization of a model material system (LFP-NaCl-CB) was realized, and the fluidization boundaries were evaluated. It was confirmed that submicron particles and nanoparticles fluidize as agglomerates with high sphericity. Furthermore, it was confirmed that agglomerates consisting of submicron and nanoparticles do indeed dynamically exchange particles. However, this only applies to particles at the surface level of the agglomerates. The VFB was unable to break agglomerates through their core, which is necessary for homogeneous mixing of the submicron sized battery materials.

Therefore, a microjet was added to the VFB and applied to both the model material system and the battery material system consisting of LIC-CB-LIC. We demonstrated that the nozzle size and its position had a significant influence on the hydrodynamics within the VFB and its ability to apply forces on the agglomerates. Based on images acquired from electron microscopy and electrochemical data, it was shown that the introduction of the microjet drastically improved the mixing capabilities of the VFB.

Therefore, in the future, the jet process will be further improved and enhanced. Numerical simulations will be used to define and optimize the stressing mechanisms in the VFB with a nitrogen jet to find the ideal conditions to produce improved ASSB cathode composites.

CRediT authorship contribution statement

Zhi Cheng Hua: Writing – original draft, Visualization, Validation, Project administration, Methodology, Investigation, Conceptualization. **Finn Frankenberg:** Writing – review & editing, Methodology, Investigation, Data curation, Conceptualization. **Maximilian Kissel:** Writing – review & editing, Visualization, Validation, Methodology, Investigation, Data curation, Conceptualization. **Jürgen Janek:** Writing – review & editing, Visualization, Supervision, Funding acquisition. **Arno Kwade:** Writing – review & editing, Visualization, Supervision, Funding acquisition, Conceptualization. **Stefan Heinrich:** Writing – review & editing, Visualization, Supervision, Project administration, Funding acquisition, Conceptualization.

Declaration of competing interest

The authors declare that they have no known competing financial interests or personal relationships that could have appeared to influence the work reported in this paper.

Funding acknowledgement

The authors would like to thank for the funding of the German Research foundation (Deutsche Forschungsgemeinschaft, DFG) in the framework SPP 2289 - 462397288, 462470125

Data availability

Data will be made available on request.

References

[1] K. Schmidt-Rohr, How batteries store and release energy: explaining basic electrochemistry, J. Chem. Educ. 95 (2018) 1801–1810, https://doi.org/10.1021/acs.jchemed.8b00479.
[2] J.T. Frith, M.J. Lacey, U. Ulissi, A non-academic perspective on the future of lithium-based batteries, Nat. Commun. 14 (2023) 420, https://doi.org/10.1038/s41467-023-35933-2.

[3] Y.-K. Sun, Promising all-solid-state batteries for future electric vehicles, ACS Energy Lett. 5 (2020) 3221–3223, https://doi.org/10.1021/acsenergylett.0c01977.
[4] X. Yu, R. Chen, L. Gan, H. Li, L. Chen, Battery safety: from lithium-ion to solid-state batteries, Engineering 21 (2023) 9–14, https://doi.org/10.1016/j.eng.2022.06.022.
[5] J. Janek, W.G. Zeier, A solid future for battery development, Nat. Energy 1 (2016), https://doi.org/10.1038/nenergy.2016.141.
[6] W. van Schalkwijk, Advances in Lithium-Ion Batteries, Springer, US, Boston, MA, 2002.
[7] M. Weiss, F.J. Simon, M.R. Busche, T. Nakamura, D. Schröder, F.H. Richter, J. Janek, From liquid- to solid-state batteries: ion transfer kinetics of heteroionic interfaces, Electrochem. Energ. Rev. 3 (2020) 221–238, https://doi.org/10.1007/s41918-020-00062-7.
[8] J. Schnell, T. Günther, T. Knoche, C. Vieider, L. Köhler, A. Just, M. Keller, S. Passerini, G. Reinhart, All-solid-state lithium-ion and lithium metal batteries – paving the way to large-scale production, J. Power Sources 382 (2018) 160–175, https://doi.org/10.1016/j.jpowsour.2018.02.062.
[9] R. Rajagopal, Y. Subramanian, K.-S. Ryu, Improving the electrochemical performance of cathode composites using different sized solid electrolytes for all solid-state lithium batteries, RSC Adv. 11 (2021) 32981–32987, https://doi.org/10.1039/d1ra05897e.
[10] F. Wei, S. Wu, J. Zhang, H. Fan, L. Wang, V.W. Lau, S. Hou, M. Zhang, J. Zhang, B. Liang, R. Zhao, Molecular reconfigurations enabling active liquid–solid interfaces for ultrafast Li diffusion kinetics in the 3D framework of a garnet solid-state electrolyte, J. Mater. Chem. A 9 (2021) 17039–17047, https://doi.org/10.1039/D1TA03569J.
[11] K.J. Kim, J.L.M. Rupp, All ceramic cathode composite design and manufacturing towards low interfacial resistance for garnet-based solid-state lithium batteries, Energ. Environ. Sci. 13 (2020) 4930–4945, https://doi.org/10.1039/D0EE02062A.
[12] F. Frankenberg, M. Kissel, C.F. Burmeister, M. Lippke, J. Janek, A. Kwade, Investigating the production of all-solid-state battery composite cathodes by numerical simulation of the stressing conditions in a high-intensity mixer, Powder Technol. 435 (2024) 119403, https://doi.org/10.1016/j.powtec.2024.119403.
[13] A. Bielefeld, D.A. Weber, J. Janek, Microstructural modeling of composite cathodes for all-solid-state batteries, J. Phys. Chem. C 123 (2019) 1626–1634, https://doi.org/10.1021/acs.jpcc.8b11043.
[14] O. Maus, M.A. Lange, F. Frankenberg, F. Stainer, V. Faka, E. Schlautmann, C. Rosenbach, A. Jodlbauer, J. Schubert, J. Janek, C. Li, P. Michalowski, H.M. R. Wilkening, A. Kwade, W.G. Zeier, Influence of post-synthesis processing on the structure, transport, and performance of the solid electrolyte Li 5.5 PS 4.5 Cl 1.5 in all-solid-state batteries, Adv. Energy Mater. (2024) 2403291, https://doi.org/10.1002/aenm.202403291.
[15] Y.J. Nam, D.Y. Oh, S.H. Jung, Y.S. Jung, Toward practical all-solid-state lithium-ion batteries with high energy density and safety: comparative study for electrodes fabricated by dry- and slurry-mixing processes, J. Power Sources 375 (2018) 93–101, https://doi.org/10.1016/j.jpowsour.2017.11.031.
[16] E. Hayakawa, H. Nakamura, S. Ohsaki, S. Watano, Dry mixing of cathode composite powder for all-solid-state batteries using a high-shear mixer, Adv. Powder Technol. 33 (2022) 103705, https://doi.org/10.1016/j.apt.2022.103705.
[17] D.H. Tan, Y.S. Meng, J. Jang, Scaling up high-energy-density sulfidic solid-state batteries: a lab-to-pilot perspective, Joule 6 (2022) 1755–1769, https://doi.org/10.1016/j.joule.2022.07.002.
[18] G. Wang, L. Chen, G.N. Mathur, V.K. Varadan, Lithium iron phosphates as cathode materials in lithium ion batteries for electric vehicles, in: Nanosensors, Biosensors, and Info-Tech Sensors and Systems 2012, SPIE, San Diego, California, 2012, p. 83440L.
[19] A.K. Padhi, K.S. Nanjundaswamy, J.B. Goodenough, Phospho-olivines as positive-electrode materials for rechargeable lithium batteries, J. Electrochem. Soc. 144 (1997) 1188–1194, https://doi.org/10.1149/1.1837571.
[20] X. Li, J. Liang, K.R. Adair, J. Li, W. Li, F. Zhao, Y. Hu, T.-K. Sham, L. Zhang, S. Zhao, S. Lu, H. Huang, R. Li, N. Chen, X. Sun, Origin of superionic Li3Y1-xInxCl6 halide solid electrolytes with high humidity tolerance, Nano Lett. 20 (2020) 4384–4392, https://doi.org/10.1021/acs.nanolett.0c01156.
[21] H. Tsukasaki, H. Sano, K. Igarashi, A. Wakui, T. Yaguchi, S. Mori, Deterioration process of argyrodite solid electrolytes during exposure to humidity-controlled air, J. Power Sources 524 (2022) 231085, https://doi.org/10.1016/j.jpowsour.2022.231085.
[22] M. Yang, L. Chen, H. Li, F. Wu, Air/water stability problems and solutions for lithium batteries, Energy Mater Adv 2022 (2022), https://doi.org/10.34133/2022/9842651, 2022/9842651.
[23] D. Geldart, Types of gas fluidization, Powder Technol. 7 (1973) 285–292, https://doi.org/10.1016/0032-5910(73)80037-3.
[24] R. Kamphorst, K. Wu, S. Salameh, G.M.H. Meesters, J.R. van Ommen, On the fluidization of cohesive powders: differences and similarities between micro- and nano-sized particle gas–solid fluidization, Can. J. Chem. Eng. 101 (2023) 227–243, https://doi.org/10.1002/cjce.24615.
[25] J.R. van Ommen, J.M. Valverde, R. Pfeffer, Fluidization of nanopowders: a review, J. Nanopart. Res. 14 (2012), https://doi.org/10.1007/s11051-012-0737-4.
[26] C. Zhu, Q. Yu, R.N. Dave, R. Pfeffer, Gas fluidization characteristics of nanoparticle agglomerates, AIChE J. 51 (2005) 426–439, https://doi.org/10.1002/aic.10319.
[27] R. Kamphorst, P.C. van der Sande, K. Wu, E.C. Wagner, M.K. David, G.M. Meesters, J.R. van Ommen, The mechanism behind vibration assisted fluidization of cohesive micro-silica, KONA (2023), https://doi.org/10.14356/kona.2024007.
[28] J.A. Quevedo, A. Omosebi, R. Pfeffer, Fluidization enhancement of agglomerates of metal oxide nanopowders by microjets, AICHE J. 56 (2010) 1456–1468, https://doi.org/10.1002/aic.12075.
[29] L.F. Hakim, J.L. Portman, M.D. Casper, A.W. Weimer, Aggregation behavior of nanoparticles in fluidized beds, Powder Technol. 160 (2005) 149–160, https://doi.org/10.1016/j.powtec.2005.08.019.
[30] J.M. Valverde Millán (Ed.), Fluidization of Fine Powders, Springer Netherlands, Dordrecht, 2013.
[31] E. Zhou, Y. Shan, L. Li, F. Shen, E. Byambajav, B. Zhang, C. Shi, Study on the fluidization quality characterization method and process intensification of fine coal separation in a vibrated dense medium fluidized bed, ACS Omega 6 (2021) 14268–14277, https://doi.org/10.1021/acsomega.1c01034.
[32] L. Fernandez-Diaz, J. Castillo, E. Sasieta-Barrutia, M. Arnaiz, M. Cabello, X. Judez, A. Terry, L. Otaegui, M.C. Morant-Miñana, A. Villaverde, Mixing methods for solid state electrodes: techniques, fundamentals, recent advances, and perspectives, Chem. Eng. J. 464 (2023) 142469, https://doi.org/10.1016/j.cej.2023.142469.
[33] D. Wei, R. Dave, R. Pfeffer, J. Nanopart. Res. 4 (2002) 21–41, https://doi.org/10.1023/A:1020184524538.
[34] J. Men, S.R. Kolan, A. Massomi, T. Hoffmann, J. Schmidt, E. Tsotsas, A. Bück, Formulation of nanostructured heteroaggregates by fluidization technologies, Chem. Ing. Tech. 95 (2023) 107–113, https://doi.org/10.1002/cite.202200139.
[35] S.R. Kolan, R. Wang, T. Hoffmann, E. Tsotsas, Mixing sub-micron particles in a ProCell type spouted bed, Powder Technol. 428 (2023) 118828, https://doi.org/10.1016/j.powtec.2023.118828.
[36] D. Schulze, Powders and Bulk Solids: Behavior, Characterization, Storage and Flow, secondnd ed, Springer International Publishing; Springer, Cham, 2021 twentiethtwenty-first.
[37] B.G. Westphal, N. Mainusch, C. Meyer, W. Haselrieder, M. Indrikova, P. Titscher, H. Bockholt, W. Viöl, A. Kwade, Influence of high intensive dry mixing and calendering on relative electrode resistivity determined via an advanced two point approach, Journal of Energy Storage 11 (2017) 76–85, https://doi.org/10.1016/j.est.2017.02.001.
[38] Y. Mawatari, T. Koide, Y. Tatemoto, T. Takeshita, K. Noda, Comparison of three vibrational modes (twist, vertical and horizontal) for fluidization of fine particles, Advanced Powder Technology 12 (2001) 157–168, https://doi.org/10.1163/15685520052384998.
[39] Y.-T. Chen, M.A.T. Marple, D.H.S. Tan, S.-Y. Ham, B. Sayahpour, W.-K. Li, H. Yang, J.B. Lee, H.J. Hah, E.A. Wu, J.-M. Doux, J. Jang, P. Ridley, A. Cronk, G. Deysher, Z. Chen, Y.S. Meng, Investigating dry room compatibility of sulfide solid-state electrolytes for scalable manufacturing, J. Mater. Chem. A 10 (2022) 7155–7164, https://doi.org/10.1039/D1TA09846B.
[40] J. Witte, Z.C. Hua, V. Kolck, H. Kruggel-Emden, S. Heinrich, E. Schmidt, Investigation of a jet-based direct mixing process for improved structuring of conductive battery hetero-agglomerates, Processes 11 (2023) 3243, https://doi.org/10.3390/pr11113243.
[41] H. Bockholt, W. Haselrieder, A. Kwade, Intensive powder mixing for dry dispersing of carbon black and its relevance for lithium-ion battery cathodes, Powder Technol. 297 (2016) 266–274, https://doi.org/10.1016/j.powtec.2016.04.011.
[42] J.K. Mayer, H. Bockholt, A. Kwade, Inner carbon black porosity as characteristic parameter for the microstructure of lithium-ion electrodes and its effect on physical and electrochemical properties, J. Power Sources 529 (2022) 231259, https://doi.org/10.1016/j.jpowsour.2022.231259.

Zhi Cheng Hua is a doctoral student at the Institute of Solid Process Engineering and Particle Technology at the Hamburg University of Technology. There, he obtained a M.Sc. in Process Engineering in 2021. His research interests include vibrated fluidized beds, nanoparticle fluidization and mixing and battery technology.

Finn Frankenberg is a doctoral student at the Institute of Particle Technology at Technical University of Braunschweig. There he obtained a M.Sc. In chemical engineering in 2023. His research interests include solid-state battery technologies, nanoparticle mixing techniques and numerical and structure simulations.

Maximilian Kissel received his M.Sc. in Materials Science from Technical University of Darmstadt in 2021. He is currently a doctoral student at the Institute of Physical Chemistry at Justus-Liebig-University in Giessen under the supervision of Prof. Jürgen Janek. His research interests include solid state batteries with a focus on process-microstructure relations in cathode composites and active material coatings.

Arno Kwade obtained his diploma in Mechanical Process Engineering and a doctoral degree at Technical University of Braunschweig. After positions as Assistant and Junior Professor and completing his Habilitation, he became a full professor at TU Braunschweig in 2005 and the executive director of the Institute for Particle Technology. He is Chair for Future Grinding Technologies at the European Cement Research Academy and leads the Mobile Energy Storage working group of the Circular Economy Initiative Germany. His main research interests include battery technology, particle simulation methods, and process engineering. He is a member of acatech and the Braunschweiger Wissenschaftliche Gesellschaft.

Jürgen Janek a professor in Physical Chemistry at Justus-Liebig University in Giessen, director of the Gießen Center for Materials Research (ZfM) and the scientific director of BELLA (Batteries and Electrochemistry Laboratory), a joint lab of BASF SE and KIT in Karlsruhe. He received his Ph.D. in Chemistry from the University of Hannover and was visiting professor at Seoul National University, Tohuku University/Sendai and Université

d'Aix-Marseille. Prof. Janek is a member of several scientific organizations and has received numerous awards, including the Greve Prize from the German National Academy of Sciences Leopoldina. Current key interests include new materials and their reactions in lithium solid-state batteries, post-lithium based next generation batteries and the defect chemistry of porous and nanostructured oxides.

Stefan Heinrich obtained his diploma in Process Engineering and a doctoral degree at the University Magdeburg. After positions as Assistant and Junior Professor and a Habilitation, he became full professor at the TUHH and director of the Institute of Solids Process Engineering and Particle Technology in 2008. He is editor of *Advanced Powder Technology* and *Particuology*, chairman of the Working Party on Agglomeration and Bulk Solids Technology of VDI-ProcessNet and of the EFCE Working Party on Agglomeration. His main research interests are fluidized bed technology, mainly for drying and particle formulation, particle simulation methods as well as contact, deformation and breakage mechanics of particles. He received the DECHEMA-Prize 2015.